HHS Public Access

Author manuscript

Glia. Author manuscript; available in PMC 2022 December 01.

Published in final edited form as:

Glia. 2021 December ; 69(12): 2812–2827. doi:10.1002/glia.24071.

Evidence for glutamine synthetase function in mouse spinal cord oligodendrocytes

Lucile Ben Haim[1,2,#], **Lucas Schirmer**[1,2,3,4], **Amel Zulji**[3], **Khalida Sabeur**[1,2], **Brice Tiret**[5], **Matthieu Ribon**[6], **Sandra Chang**[1,2], **Wouter H. Lamers**[7], **Séverine BoillEée**[6], **Myriam M. Chaumeil**[5], **David H. Rowitch**[1,2]

[1]Department of Pediatrics, Wellcome - MRC Cambridge Stem Cell Institute, University of Cambridge, Cambridge, UK

[2]Departments of Pediatrics and Neurosurgery, Eli and Edythe Broad Center of Regeneration Medicine and Stem Cell Research, University of California, San Francisco, San Francisco, CA, USA

[3]Department of Neurology, Mannheim Center for Translational Neuroscience, Medical Faculty Mannheim, Heidelberg University, Mannheim, Germany

[4]Interdisciplinary Center for Neurosciences, Heidelberg University, Heidelberg, Germany

[5]Departments of Physical Therapy and Rehabilitation Science and of Radiology and Biomedical Imaging, University of California, San Francisco, CA, USA

[6]Sorbonne Université, Institut du Cerveau - Paris Brain Institute - ICM, Inserm, CNRS, APHP, Hôpital de la Pitié Salpêtrière, Paris, France

[7]Tytgat Institute for Liver and Intestinal Research, Amsterdam University Medical Centers, Meibergdreef 15, 1105 BK Amsterdam, The Netherlands

Abstract

Glutamine synthetase (GS) is a key enzyme that metabolizes glutamate into glutamine. While GS is highly enriched in astrocytes, expression in other glial lineages has been noted. Using a combination of reporter mice and cell type-specific markers, we show that GS is expressed in myelinating oligodendrocytes (OL) but not oligodendrocyte progenitor cells of the mouse and

Correspondence: Lucile Ben Haim (lucile.ben-haim@cea.fr), David H. Rowitch (dhr25@medschl.cam.ac.uk).
[#]Current affiliation: Université Paris-Saclay, CEA, CNRS, MIRCen, Laboratoire des Maladies Neurodégénératives, 92265, Fontenay-aux-Roses, France

Author contributions

L.B.H. conceived the project, designed and performed the experiments, wrote the manuscript and designed the figures. L.S. provided performed human tissue staining and imaging, helped with performing OPC immunopanning experiments and edited the manuscript. A.Z. performed bioinformatics analysis of published sc/snRNA-seq data sets and generated plots. B.T. performed ^{1}H-NMR experiments on spinal cord extracts. K.S. helped with behavioral testing and histological tissue processing. S.C. was in charge of mouse genotyping. M.R and S.B. provided time course samples from SOD1(G93A) mice. W.H.L. provided the *Glul*$^{fl/fl}$ mice. M.M.C. analyzed ^{1}H NMR data and edited the manuscript. D.H.R supervised the project and helped write the manuscript.

Conflict of interests

Authors declare no conflict of interest.

Data and material availability statement

All unique reagents/materials generated in this study will be available by contacting the corresponding authors upon completion of pertinent material transfer agreement. This study did not generate any code.

human ventral spinal cord. To investigate the role of GS in mature OL, we used a conditional knockout (cKO) approach to selectively delete GS-encoding gene (*Glul*) in OL, which caused a significant decrease in glutamine levels on spinal cord extracts. *GS* cKO mice (*CNP-cre*$^{+}$*:Glul*$^{fl/fl}$) showed no differences in motor neuron numbers, size or axon density; OL differentiation and myelination in the ventral spinal cord was normal at 1 and 6 months. Interestingly, *GS* cKO mice showed a transient and specific decrease in peak force while locomotion and motor coordination remained unaffected. Last, GS expression in OL was increased in chronic pathological conditions in both mouse and humans. We found a disease-stage dependent increase of OL expressing GS in the ventral spinal cord of *SOD1(G93A)* mouse model of ALS. Moreover, we showed that *GLUL* transcripts levels were increased in OL but not in astrocytes in leukocortical tissue from multiple sclerosis but not control patients. These findings provide evidence towards OL-encoded GS functions in spinal cord sensorimotor axis, which is dysregulated in chronic neurological diseases.

Graphical Abstract

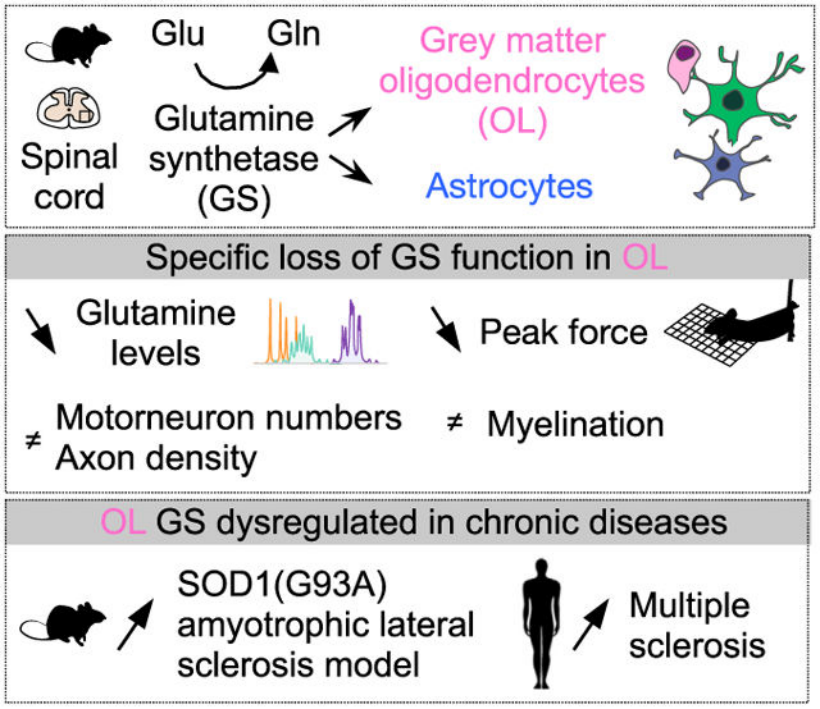

Keywords

Oligodendrocytes; glutamine synthetase; spinal cord; motor neurons; peak strength; amyotrophic lateral sclerosis

Introduction

Glutamine synthetase (GS) is an ATP-dependent enzyme, which catalyzes the transformation of glutamate (Glu) and ammonium into glutamine (Gln) (Mates, Campos-

Sandoval, Santos-Jimenez, & Marquez, 2019). It is involved in maintaining Gln physiological levels and in the rapid recycling of Glu through the “Glu-Gln cycle”, which is crucial for excitatory neurotransmission (Daikhin & Yudkoff, 2000; Norenberg & Martinez-Hernandez, 1979). In the central nervous system (CNS), GS has generally been considered an astrocyte-specific enzyme, especially in forebrain regions (Liang, Carlson, & Coulter, 2006; Papageorgiou et al., 2018). Loss-of-function of GS-encoding gene, *Glul*, leads to major cerebral abnormalities in humans, decreased Gln levels (Haberle et al., 2005) and early neonatal death in mice (He et al., 2010). Astrocyte-specific GS expression is altered in many pathological conditions including neurodegenerative diseases, hypoxia or epilepsy both at the gene and protein levels (Jayakumar & Norenberg, 2016; Rose, Verkhratsky, & Parpura, 2013; Xin et al., 2019). While GS expression has also been reported in oligodendrocytes (OL) of brain and spinal cord white matter (Bernstein et al., 2014; Cammer, 1990; D'Amelio, Eng, & Gibbs, 1990; Takasaki et al., 2010; P. Werner, D. Pitt, & C. S. Raine, 2001), *Glul* function in oligodendroglia is less understood and even controversial (Anlauf & Derouiche, 2013). Yet, recent evidence convincingly showed that GS in OL was important for glutamatergic transmission in the mouse midbrain (Xin et al., 2019). Given the key role of GS function in neuron-glia crosstalk, we investigated its cell type-specific expression in oligodendroglia both in human and mouse spinal cord and focused on its function in the mouse sensorimotor axis.

Material and methods

Mice.

All mouse strains except the *SOD1(G93A)* were maintained at the University of California, San Francisco (UCSF) pathogen-free animal facility and all animal protocols were approved by and in accordance with the guidelines established by the Institutional Animal Care and Use Committee and Laboratory Animal Resource Center under protocol number AN110094. *Aldh1l1-eGFP* (OFC789Gsat/ 011015-UCD) transgenic mice were generated by the GENSAT project (Gong et al., 2003) and *MOBP-eGFP* mice (IN1Gsat) were obtained from MMRRC and maintained as homozygous on a C57BL/6J background. *Glul* $^{fl/fl}$ mice were obtained from Dr. W. H. Lamers (Amsterdam University Medical Centers) (He et al., 2010). Previously characterized *CNP-cre* transgenic mice were originally developed in Pr. K-A. Nave lab (Lappe-Siefke et al., 2003) and obtained from the JAX (# 3051635). *NG2-DsRed* mice (Tg(*Cspg4-DsRed.T1*)1Akik) were developed by Dr. A. Nishiyama (University of Connecticut) (Zhu, Bergles, & Nishiyama, 2008) and obtained from Dr. S. Fancy (UCSF). *Glul*$^{fl/fl}$ mice were bred with *CNP-cre : Glul*$^{fl/+}$. *CNP-cre*$^{-}$ *: Glul*$^{fl/fl}$ or $^{fl/+}$ where used as controls and *CNP-cre*$^{+}$ *: Glul*$^{fl/fl}$ as cKO. For clarity, *CNP-cre*$^{+}$ *: Glul*$^{fl/fl}$ will be abbreviated as *GS* cKO in the manuscript. Specific genotyping information can be found in (He et al., 2010). *SOD1(G93A)* mice (*B6.Cg- Tg(SOD1*G93A)1Gur/J-* JAX # 004435) were hemizygous for a 12kb genomic fragment encoding the human mutated *SOD1* gene under its endogenous promoter and develop an ALS-like phenotype including a progressive paralysis (Gurney et al., 1994). Specific genotyping information are described in (Chiot et al., 2020). For *SOD1(G93A)* mice, animal procedures (including endstage definition) were performed in accordance with the guidelines for care and use of experimental animals of the European Union and approved by the ethics committee for animal experimentation n°5

in Ile-de-France to the UMS28, Centre d'expérimentation fonctionnelle, Paris, France. Mice were monitored weekly from the pre-symptomatic stage (50 days) until disease endstage (around 165 days) to assess signs of paralysis, grip strength (Bioseb, grip test; average of three consecutive weekly measures) and weight. Disease time points were defined as previously described (Chiot et al., 2020). Disease onset was retrospectively determined as the age mice reached either peak body weight or peak grip strength (102 days); early disease was defined as the age at which animals had lost 10% of their maximal weight or 35% of their maximal grip strength (146 days). This early disease stage was followed by the appearance of progressive paralysis. The late symptomatic stage was considered when mice had lost 15% of their maximal weight. This stage was characterized by the beginning of hindlimb paralysis, walking difficulties and inability to perform the grip test. During the symptomatic phase, mice were monitored at least twice a week and daily near endstage, which was defined by severe paralysis (impossibility to right itself within 20 seconds when placed on its side, an endpoint frequently used for *SOD1(G93A)* mice expressing mice). Endstage was reached at an average of 167 days.

All mice were maintained on a 12-hour light/dark cycle with food and water available *ad libitum*. For all experiments except with *SOD1(G93A)* mice, littermates were randomly assigned to experimental groups with approximately equal amounts of males and females. No significant effect of sex was observed in data analyses. For experiments involving *SOD1(G93A)* mice, only females were used since we kept all males for breeding purposes.

Human tissue.

Human spinal cord samples were obtained from the UK Multiple Sclerosis Tissue Bank at Imperial College, London. Three snap-frozen control human tissues from deceased individuals without spinal cord pathology (Supp. Table 1) were obtained via a prospective donor scheme following ethical approval by the National Research Ethics Committee in the UK (08/MRE09/31). We have complied with all relevant ethical regulations regarding the use of human postmortem tissue samples.

Immunofluorescence stainings.

Mice were deeply anesthetized and transcardially perfused with 4% paraformaldehyde (PFA). Vertebral columns were isolated, post-fixed in 4% PFA for 24h followed by cryoprotection in 30% sucrose diluted in 0.1M PBS for 48h at 4°C samples. Spinal cords were dissected out, cut in segments corresponding to different anatomical levels (from cervical to sacral) and embedded in optimal cutting temperature compound (Tissue-Tek). Spinal cords segments were cut using a cryostat (CM3050S, Leica) and serially collected on Superfrost® slides (VWR) (14-16µm-thick sections) or as free-floating sections (30µm-thick) in P24 well plates in cryoprotecting solution and stored at −20°C. Cryosections were subjected to antigen retrieval by pre-treatment in 1X Dako Target solution for 2 min at 95°C in a microwave oven (BioWave). Sections were then permeabilized and blocked in 0.1M phosphate buffered saline (PBS)/0.2% Triton X (TX)-100/10% horse serum (HS) for 1h at room temperature (RT). Primary antibody incubations were carried out overnight at 4 °C. After washing in 0.1M PBS, sections were incubated with secondary antibodies diluted

in 0.1M PBS/ 0.2% TX-100/10% HS for 1h, RT. Goat or donkey Alexa Fluor -tagged secondary IgG (H+L) antibodies were used for primary antibody detection (Thermo Fisher Scientific, 1:500). After rinsing, slides were mounted with Fluoromount-G™ Mounting Medium, with DAPI (SouthernBiotech). For free-floating sections, protocols were identical except that sections were rinsed twice in 0.1M phosphate buffer for 48h to remove traces of storing solution, no antigen retrieval was performed and 4.5% normal goat serum was used for blocking and antibody incubations. Sections were incubated with DAPI (1:5000) for 5 min in 0.1M PBS and rinsed before being mounted on SuperFrost® Plus (ThermoFisher Scientifc) slides and coverslipped with Fluorsave™ (Calbiochem, Darmstadt, Germany) medium.

For human tissue processing, frozen sections were fixed in 100% ice-cold methanol for 5 min, rinsed in 0.1M PBS/0.1% TX-100/5% HS and incubated overnight at 4°C with primary antibodies in 0.1M PBS/0.1% TX-100/5% HS. Sections were then rinsed and incubated with secondary antibodies in 0.1M PBS/0.1% TX-100/5% HS for 30 min. Sections were then rinsed and mounted with Fluoromount-G™ Mounting Medium, with DAPI. Primary antibodies used included: mouse anti-APC (clone CC1, OP80, 1:300, Millipore), rabbit anti-AQP4 (AB3594, Millipore, 1:500), rabbit anti-Calbindin D-28k (CB-38a, Swant, 1:500), goat anti-ChAT (AB144P, Millipore, 1:200), rat anti-GFAP (13-0300, Invitrogen, 1:1,000), anti-GFAP-Cy3 (C9205, Sigma, 1:1,000), rabbit anti-GS (G2781, Sigma, 1:1,000, antibody directed against C-term AA 357-363 with N-terminally added Lys), mouse anti-GS (MAB302, clone GS-6, Millipore, 1:1,000), rabbit anti-IBA1 (019–19741, Wako, 1:500), rat anti-MBP (ab7349, Abcam, 1:500), mouse anti-NeuN (MAB377, Millipore, 1:1,000), mouse anti-Neurofilament H, nonphosphorylated (clone SMI32, 801701, Biolegend, 1:10,000), mouse anti-Neurofilament H, phosphorylated (clone SMI312, 837904, Biolegend, 1:1,000), mouse anti-NOGO-A (clone 11C7, gift from Dr. M.E. Schwab to L.S., 1:3,000), goat anti-Olig2 (AF2418, R&D Systems, 1:50), rabbit anti-Parvalbumin (PV25, Swant, 1:500), rabbit anti-PDGFRα (3164, Cell Signaling, 1:100), guinea pig anti-VGLUT1 (AB5905, Millipore, 1:5,000), guinea pig anti-VGLUT2 (AB2251, Millipore, 1:5,000).

Image acquisition and analysis.

Images were acquired using an epifluorescence microscope Zeiss Axio Imager (10x objective) or confocal microscopes Leica TCS SPE or SP8 (20x or 40x objectives). All images within one experimental cohort were obtained from samples processed in a strictly identical manner and acquired using the same settings across experimental groups. Image analysis was performed using Image J (National Institutes of Health, https://fiji.sc/ or https://imagej.nih.gov/ij/). For epifluorescence images, cell numbers and mean grey values (immunoreactivity) were quantified on an average of 5 serial spinal cord hemisections per mouse on manually-drawn region of interest. For confocal images, quantifications were performed on 3-4 fields in the ventral spinal cord grey matter, on 3 consecutive serial sections on maximum intensity projection images. MN soma size was measured as described previously (Kelley et al., 2018). Image J threshold function was used to quantify the % of $GFAP^+$ and $IBA1^+$ area on stacked confocal images and combined the analyze particles function for automatic quantification of the numbers of GS^+ and GFP^+ cell bodies on

epifluorescence images on manually-drawn regions of interest corresponding to spinal cord sub-compartments.

Quantitative RT-PCR.

RNA was isolated using Trizol reagent (Invitrogen), DNase-digested to remove genomic DNA and purified using the RNAeasy Kit (Qiagen) according to manufacturer's instructions. Complementary DNA was generated using SuperScript™ III One-Step RT-PCR System with Platinum™ Taq DNA Polymerase (Invitrogen). qPCR was performed by using LightCycler 480 SYBR Green I Master mix Roche (Roche) with specific primers designed for 75–150 bp amplicons using Primer 3. The following primer sequences were used: *Glul* (F: GGGCTACTTTGAAGACCGTC; R: TTCGTCGCCTGTTTCGT), *Pdgfra (F: GGCCAGAGACATCATGCACGATTC ; R : TCAGCGTGGTGTAGAGGTTGTCGAA*), *Mbp* (F: CCCAAGGCACAGAGACACGGG; R: TACCTTGCCAGAGCCCCGCTT), and *18S* (F: GTTCCGACCATAAACGATGCC; R: TGGTGGTGCCCTTCCGTCAAT). *18S* was used as housekeeping gene and melting curve analyzed to ensure correct and specific amplification.

Western blot.

Mouse brainstem tissue (pons and medulla oblongata) samples were dissected. Sample lysis was performed in RIPA buffer (Thermofisher) in the presence of protease and phosphatase inhibitors (Cell signaling). Samples concentration was determined with the Bradford method and protein migration and gel transfer was performed as described previously (Kelley et al., 2018). After blocking in Odyssey® Blocking Buffer (PBS) (Li-Cor) for 1h at RT, primary antibodies were incubated overnight at 4°C onto the blotting membrane. The following antibodies were used: rabbit anti-GS, rat anti-MBP and mouse anti-Tubulin β 3 (MMS435P, Covance, 1:10000). IRDye® Goat anti-mouse, anti-rat and anti-rabbit (680 and 800) fluorescent secondary antibodies (Li-cor) were used for protein detection on the Odyssey Cxl imaging system.

Ex vivo ^{1}H NMR.

Metabolites from mouse whole spinal cord were extracted using equal parts methanol-water-chloroform, as previously described (Tyagi, Azrad, Degani, & Salomon, 1996). Briefly, animals were euthanized and 89 ± 5mg of spinal cord tissue collected and snap-frozen in liquid nitrogen. Using a mortar and pestle, frozen tissue was homogenized in −20°C methanol. Equal parts −20°C chloroform and 4°C H_2O were homogenously mixed, and the fractions separated by centrifugation at 125g at 4°C. Upon collection of the methanol fraction, 11.7mM Trimethylsilylpropanoic acid (Acros Organics) was added and the mixture lyophilized. The resultant extracts were reconstituted in 420μL distilled H_2O and samples were scanned on a 500Mhz NMR system (Bruker) with a 1D pulse acquire zgpr sequence (NS = 16, DS 2, 32k datapoint, TR 2sec). Glutamine and glutamate and were fitted and quantified after normalization to N-acetyl aspartate (NAA) using Chenomx NMR Suite (Chenomx Inc) with reference to the Human Metabolomics Database (Wishart et al., 2018).

Behavioral analysis.

All behavioral experiments were performed at the UCSF Neurobehavioral Core for Rehabilitation Research. Mice were habituated to the experimenter through handling, weighting and cage change starting one week prior to behavioral testing. Experiments were all performed at the same time of the day for each day of testing. The rotarod test (Ugo Basile) was performed to assess motor coordination and motor learning. Mice were placed onto a rotating rod accelerating from 0-40 rotations per minute during 5 minutes. Animals were tested 3 times per day (T1, T2, T3) for 3 consecutive days (D1, D2, D3) and the latency to fall from the apparatus at each trial was measured. Forelimb grip strength was measured using a grip strength apparatus (Bioseb). The grip strength of each mouse was measured on 3 trials per day for 3 consecutive days and the average peak force per animal was computed. The open field test (Kinder-Scientific) was used to assay overall locomotor activity. Mice were let to freely explore an open arena connected to a video tracking software for 10 min. Data collected includes distance traveled and number of rearings (exploratory behavior where mice stands on its hind legs).

OPC immunopanning.

Cells were isolated from neonatal mouse cortices using anti-PDGFRα (anti-CD140a, 558774, BD Biosciences) immunopanning antibody for positive selection of OPCs (Yuen et al., 2014). Briefly, OPCs were immunopanned from P7-P9 mouse cortices and plated on poly-D-lysine coverslips (Neuvitro). Cells were kept in proliferation media (PDGF-AA, CNTF, and NT3; Peprotech) at 10% CO_2 and 37°C. After two days in proliferation media, differentiation was induced by changing media to contain CNTF and triiodothyronine (T3; Sigma). RNA extraction was performed on OL after 48h in differentiation media. Mycoplasma contamination testing was negative.

Bioinformatic analysis of existing data sets.

Normalized and scaled data sets (feature-barcode matrices) from published mouse spinal cord single-cell RNA sequencing (scRNA-seq) (Blum et al., 2021) and human leukocortical single-nucleus RNA-sequencing (snRNA-seq) (Schirmer et al., 2019) and tissues were obtained (https://cells.ucsc.edu/ and http://spinalcordatlas.org/) and used without any processing. In addition, another mouse CNS scRNA-seq data sets (Marques et al., 2016) was reconstructed using the available count matrix and corresponding metadata (GSE75330). It should be noted that 16 cells in the metadata and matrix did not match, so these cells were omitted from the downstream analysis (Supp. Table 2). Briefly, the count matrix was transformed using SCTransoform (Hafemeister & Satija, 2019) as part of the Seurat toolkit (Stuart et al., 2019). The dimensionality of the data was reduced using principal component analysis (PCA) and the first 18 PCs were used for downstream clustering analysis. Cells were annotated using inferred cell identities provided by the authors in the metadata.

Statistical analysis.

We pre-determined group sample size based on previously published studies. Individual experimental values are shown on bar plots and no data were excluded from analysis. All bar graphs are expressed as mean ± SEM. In box-and-whisker plots, center lines indicate

medians, box edges represent the interquartile range, and whiskers extend down to the 10th and up to the 90th percentiles of the distribution. Data sets normality was assessed using the Shapiro-Wilk test. Two-tailed unpaired parametric or non-parametric (Mann-Whitney test) t-tests were performed for two group comparisons. Data sets with n=3 were analyzed with parametric tests as the non-parametric equivalents rely on ranking, which is not reliable for small sample size (GraphPad Prism 8). Repeated measures (genotype * time) ANOVA or mixed effects model (if missing values) tests were to analyze grip strength and rotarod experiments. Level of significance was determined as described in individual figure legends. P values were designated as follows: *p<0.05, **p<0.01, ***p<0.001. All statistical tests were performed using GraphPad Prism 9 (GraphPad Software).

Results

Macroglial-specific GS expression in the mouse spinal cord.

We first wanted to establish the precise pattern of GS expression in macroglial cells (astrocytes and OL lineage cells). We detected GS by immunofluorescence staining in the astrocyte transgenic mouse reporter *Aldh1L1-eGFP* (Figure 1A). The visualization of the entire astrocytic morphology (soma and cytoplasmic processes) in *Aldh1L1-eGFP* samples allowed us to show that astrocytes represent around 40% of all cells expressing in their soma + processes, which corresponds to ~75% of all *Aldh1L1-eGFP*$^+$ astrocytes (Figure 1B). Astrocytic GS expression was confirmed using a co-immunofluorescence staining of GS and astrocyte markers aquaporin 4 (AQP4) and glial acidic fibrillary protein (GFAP) (Figure 1C). A high number of GS$^+$ cell bodies did not co-localize with astrocyte markers. These cell bodies were identified as mature OL as they co-localized with eGFP in mature myelinating OL reporter mice (*MOBP-eGFP*) (Figure 1D). In fact, around 80% of all GS$^+$ cell bodies are OL in the ventral grey matter, which accounted for ~65% of all *MOBP-eGFP*$^+$ OL (Figure 1D). We further confirmed that GS was expressed in mature OL identified by co-expression of OL-specific markers CC1 and Olig2 (Figure 1F-H). This expression pattern was observed using two antibodies from different suppliers which gave the same results except that the astrocytic GS expression in fine cytoplasmic processes was more prominent with the G2781 rabbit anti-GS antibody (Supp. Figure 1). The onset of GS expression in CC1$^+$ OL was between postnatal day (P) 14 and 40 (Supp. Figure 2A, B). Interestingly, GS expression appeared to be conserved between mouse and human CNS at the protein level as we found that some GS$^+$ cells co-localized with NOGO-A$^+$, an established OL marker but not GFAP in the ventral horn of human spinal cord sections (Figure 1I). These findings indicate that GS is expressed prominently in astrocytes and mature OL in the mouse and human spinal cord.

We further investigated GS cell-type specific expression in the mouse spinal cord. We performed immunofluorescence co-stainings of GS with the OPC marker PDGFRα on WT mice or detected GS on spinal cord sections from *NG2-DsRed* OPC reporter mice. We found no expression of GS in OPCs (Figure 2A). Furthermore, using OPC immunopanning, we found that *Glul* transcript levels were higher in differentiation (mature OL) as compared to proliferation (OPCs) conditions. *Pdgfra* and *Mbp* transcript levels were used as positive control markers for proliferation (OPCs) and differentiation (OL) conditions, respectively

(Figure 2B). We also analyzed *Glul* expression in cells of the OL lineage from a published single cell RNA sequencing data set (scRNA-seq; mouse CNS; Marques et al. (2016)) (Figure 2C, D). In keeping with our results at the transcript and protein levels, *Glul* was enriched in mature OL (MOL) clusters 1 to 6 and its expression profile clearly resembled the mature myelinating OL marker, *Mobp* (Figure 2D). By contrast, *Glul* expression level was low in newly formed OL and OPC clusters, identified with *Pdgfra*. (Figure 2D). These findings were consistent with *Glul* enrichment analysis in a published single nuclei (sn) RNA-seq data set from adult mouse spinal cord (Blum et al., 2021) (Figure 2E). We found that *Glul* was expressed in two main cell populations: mature OL, identified with *Mobp* and astrocytes (AS), identified with *Aqp4* expression. Some endothelial cells (*Flt1*) expressed *Glul* transcripts but it was not detected in microglia (*Cx3Cr1*) and neurons (*Rbfox3*) (Figure 2F). We confirmed that no expression of GS was detectable in $NeuN^+$ neurons or in $IBA1^+$ microglia at the protein level in the mouse ventral spinal cord (Figure 2G). Last, these findings were conserved between human and mouse spinal cord tissue as analyzing a published snRNA-seq data set from human leukocortical tissues (Schirmer et al., 2019), we found that *GLUL* was prominently expressed both in astrocytes (*AQP4*) and mature OL (*MOBP*) as compared to microglia (*DOCK8*), inhibitory (*GAD1*) or excitatory neurons (*SV2B*) (Figure 2H, I). Together, these results show that GS expression is macroglial-specific in the ventral spinal cord and that in oligodendroglia, it is expressed in mature OL rather than OPCs.

Topographical distribution of GS>$^+$ OL in the mouse spinal cord.

We next examined the distribution of GS^+ OL in the mouse spinal cord. As shown in Figure 3A, B, GS^+ OL are present along the spinal cord rostro-caudal axis at lumbar and cervical spinal cord levels. To determine if the density of GS^+ OL was enriched in specific spinal cord areas, we quantified the numbers of GS^+ and GFP^+ cell bodies in manually-drawn region of interest in the dorsal grey matter (DGM), the ventral grey matter (VGM), the dorsal white matter (DWM) and ventral white matter (VWM) of *MOBP-eGFP*$^+$ mice (Figure 3C). The number of GS^+ OL cell bodies was increased in grey versus white matter areas and within the grey matter, in ventral as compared to dorsal subcompartments (Figure 3D). By contrast, numbers of GFP^+ cell bodies were similar in dorsal and ventral grey matter, as the reporter labeled all OL, which are homogenously distributed in these compartments. Unsurprisingly, the numbers of GFP^+ OL were higher in the white versus grey matter (Figure 3E). It is to note that dorsal horn was excluded from the analysis, as GS is highly expressed in astrocyte processes, preventing GS^+ OL cell bodies counts.

Interestingly, by contrast to astrocytes, grey matter GS^+ OL can display a perineuronal localization. Yet, this did not seem to be neuron subtype-specific as GS^+ OL were found around $ChAT^+$ motor neurons (MN), $Parvalbumin^+$ (PV) and $Calbindin^+$ (Calb) interneurons (Figure 3F). We found that more than half of the total MN cell bodies were contacted by GS^+ OL, which represented about 15% of all GS^+ OL (Figure 3G, H). As GS metabolizes Glu, we next determined if GS^+ OL would topographically cluster according to glutamatergic terminals that are abundant in the mouse ventral spinal cord. However, using immunofluorescence co-stainings of GS and glutamatergic terminal markers VGLUT1

and VGLUT2, we found no obvious co-clustering of GS^+ OL with glutamatergic synapses (Figure 3I).

OL-specific GS loss of function does not lead to prominent histological alterations.

We next used a conditional knockout (cKO) approach to investigate the functional role of GS-encoding gene, *Glul* and focused on its consequences on the mouse ventral spinal cord. We used *CNP-cre* to selectively remove *Glul* in mature OL, by breeding *Glul* $^{fl/fl}$ *mice* with *CNP-cre* mice, as previously described (Lappe-Siefke et al., 2003) (Figure 4A). *CNP-cre* $^{+}$*: Glul* $^{fl/fl}$ (hereafter called *GS* cKO) mice showed almost complete elimination of GS^+ OL in the mouse ventral horn as compared to *CNP-cre*$^-$ (controls) (Figure 4B). Despite this, the ratio of $Olig2^+/CC1^+$ cell numbers reflecting OL differentiation was not different between *GS* cKO and controls, suggesting that it was not impacted by the loss of GS expression in OL (Figure 4C). In addition, GS protein levels, as detected by immunofluorescent staining (Supp. Figure 3A) and western blotting on ventral brain (pons and brainstem) samples, was decreased but not abolished since GS is still expressed by astrocytes (Supp. Figure 3B). We confirmed that *GS* cKO efficiency was stable in time as similar results were obtained in 1 and 6 months-old (mo) mice (Supp. Figure 3C). Because GS is also expressed in astrocytes, we checked whether the loss of GS expression in OL could lead to a compensatory upregulation by astrocytes. Thus, we compared GS immunoreactivity in $CC1^-$ cells in 1 mo *GS* cKO and control mice and found no significant differences in GS astrocytic signal in the ventral spinal cord grey matter (Supp. Figure 3D, E).

GS metabolizes Glu into Gln. To determine whether GS loss in OL has functional effects on Glu and Gln levels, we used ^{1}-H nuclear magnetic resonance (NMR)- based metabolomic analysis of spinal cord extracts from 2 mo *GS* cKO and control mice (Figure 4D). We found that the Gln/Glu ratio was decreased in *GS* cKO and that Gln but not Glu levels were significantly decreased, as normalized to N-acetyl-aspartate (NAA) (Figure 4E). The same results were obtained when using another metabolite for normalization (myoinositol). This result confirms that GS loss of function in OL has a functional role in metabolizing Glu into Gln in the mouse spinal cord.

We next investigated the effect of GS loss of function at the cellular level in the ventral spinal cord. As shown in Figure 5A-C, we found no difference in $ChAT^+$ MN numbers and soma area in *GS* cKO mice and controls at 1 or 6 months of age. Ventral grey matter MN did not show signs of acute dysfunction as we did not observe a loss of Neurofilament H, nonphosphorylated (SMI32) immunoreactivity in MN cell bodies, which is often used as a marker of dysfunction (Figure 5D). Conversely, density and diameter of $SMI312^+$ axons in ventral spinal cord white matter was similar between *GS* cKO and littermate controls at 1 and 6 months of age (Figure 5E, F). Myelin content as detected with MBP expression was also unchanged in *GS* cKO at 1 and 6 months (Figure 5E, G). Consistent with this result, we found no evidence of neuroinflammation in the ventral spinal cord grey matter (Supp. Figure 3F). Indeed, immunoreactivity levels of $GFAP^+$ astrocytes and $IBA1^+$ microglia (Supp. Figure 3G, H) were comparable between *GS* cKO and control mice. Together, these results showed that the loss of GS expression in OL does not trigger detectable histological alterations as late as 6 months of age.

Transient decrease in peak force in *GS* cKO mice.

We investigated motor behavior in *GS* cKO mice and littermate controls from 2 to 6 months of age (Figure 6). We first used the grip strength test to measure forelimb peak force in *GS* cKO and control mice at different time points (2, 4 and 6 months of age) (Figure 6A). Male and female performances per genotype were not different, so both genders were pooled for each time points. Surprisingly, peak force was significantly decreased at 2 and 4 but this difference was not maintained at 6 months. To determine whether this behavior was specific to peak force, we assessed motor coordination and motor learning using the rotarod test (Figure 6B). We found no differences between the performances of *GS* cKO mice and controls at 2.5 and 4.5 months. Finally, we used the open field test to assess general locomotor function (Figure 6C). There was no significant difference in the total distance moved and number of rearings between *GS* cKO mice and controls, even at 6 months of age. Together, these results showed that GS loss-of-function in OL results in a transient and specific loss of peak force in young mice.

GS expression in OL is dysregulated in progressive neurological diseases.

While the genetic ablation of GS-encoding gene in OL was tolerated, we next wanted to investigate whether OL GS could be dysregulated in pathological conditions. First, we studied GS expression profile in the mutant superoxide dismutase (SOD) 1 ((G93A)) mouse model of amyotrophic lateral sclerosis (ALS) (Gurney et al., 1994), which is characterized by a progressive and prominent loss of MN in the ventral spinal cord. We found a significant increase in the number of GS^+ cell bodies in SOD1(G93A) mice as compared to age-matched littermate controls in endstage animals, as showed by extensive loss of $NeuN^+$ neurons in ventral spinal cord grey matter as well as a tendency for GS IR per OL to increase (Figure 7A, B). We next evaluated how GS expression changed according to disease progression using SOD1(G93A) spinal cord samples from four distinct time points: presymptomatic, early symptomatic, late symptomatic and endstage. We found that there was a disease-stage dependent increase in GS^+ cell body numbers (Figure 7C, D), which was significantly correlated with microglial activation (Suppl. Figure 4A, B, D, E) and astrocyte reactivity (Suppl. Figure 4A, C, F, G). Second, we wanted to determine if GS OL dysregulation was also observed in human disease. We analyzed *GLUL* expression levels in a published snRNA-seq data set from human leukocortical tissues in multiple sclerosis (MS) and non-MS controls (Schirmer et al., 2019). We found that *GLUL* levels were significantly upregulated in remaining OL but not astrocyte nuclei in MS samples as compared to controls. Together, these results suggest that GS expression levels are increased in various progressive CNS pathological conditions both in humans and mouse models.

Discussion

While prior studies have reported expression of GS in the mammalian CNS (Bernstein et al., 2014; Cammer, 1990; D'Amelio et al., 1990; Takasaki et al., 2010; Xin et al., 2019), we have significantly extended this analysis focusing on the spinal cord in both mouse and human. We showed that OL lineage-specific GS function is required for normal peak strength in young animals. Last, we described that OL-specific GS expression is dysregulated in chronic neurological diseases both in mouse and humans.

Using a combination of immunofluorescence detection with cell type-specific markers and transgenic reporter mice, we showed that, in the ventral spinal cord grey matter, GS is highly expressed in OL cell bodies and astrocytes but not in OPCs, neurons or microglia. Importantly, a similar expression pattern was observed in human control spinal cord samples. Immunodetection of GS in our hands was robust as (i) we obtained identical results with two commercial antibodies and (ii) signal that was lost upon OL lineage cKO in *Glul* $^{fl/fl}$ mice (*CNP-cre* and *Olig2-cre* (data not shown)), demonstrating specificity. At the transcript levels, *Glul* was enriched in OL and astrocytes and this pattern was largely conserved between mouse and human CNS. Interestingly, re-analyzing a published RNAseq data set from adult mouse spinal cord (Blum et al., 2021), we found that *Glul* transcripts were also detected in endothelial cells. This result is in accordance with a recent study showing that GS function in endothelial cells is required for neonatal vascular development in the retina and pathological angiogenesis but it has never been investigated in the spinal cord (Eelen et al., 2018). In the peripheral nervous system, GS can be detected in Schwann cells and satellite glial cells at the protein (Miller, Richards, & Kriebel, 2002) and transcript (Avraham et al., 2020) levels. Altogether, these results suggest a robust expression pattern for GS, in the nervous system parenchyma, not only in astrocytes but also in other glial cells involved in providing neurons with metabolic support.

Given that GS is expressed in different cell types, we used a cKO approach to investigate its function specifically in mature OL using the *CNP-cre* mouse line. Gln levels were significantly decreased whereas Glu levels were unchanged, translating into a decreased Gln/Glu ratio as measured with *ex vivo* ^{1}H-NMR. These results are consistent with previous findings obtained by high performance liquid chromatography in early postnatal glial *KO* mice (*human GFAP-Cre* $^{tg/-}$*/Glul* $^{fl/LacZ}$) (He et al., 2010). In another recent study, GS expression and function was characterized in midbrain OL using a distinct OL-targeting *cre* mouse line (*iMOG-cre*) (Xin et al., 2019). They found that both Gln and Glu levels, as detected by colorimetric assay, were decreased in cKO mice as compared to controls. These discrepancies could be due to the different methods used to measure tissue metabolites and/or to local differences of GS activity in different CNS regions. Importantly, the rest of our findings are largely in accordance with the latter study, mainly conducted in the midbrain.

GS cKO mice showed a significant decrease in forelimb peak force at 2 and 4 months of age. This effect appears specific to forelimb muscle force as overall motor coordination and rearing behavior (involving hindlimbs) were not altered in *GS* cKO mice at 2.5 and 4.5 months. We found that MN numbers, axon density and myelination were comparable in *GS* cKO and controls at both 1 and up to 6 mo. Thus, the observed behavioral effect cannot be explained by detectable alterations at the histological level. Although these histology-based approaches have been used in the past to evidence MN loss (Molofsky et al., 2014), they might not be sensitive enough to detect subtle changes. In addition, it is possible that MN stress rather than death might be at play in *GS* cKO mice. Furthermore, it is likely that MN electrophysiological properties rather than numbers are altered in *GS* cKO mice. Unfortunately, we did not pursue these experiments as they are experimentally very challenging to perform in the adult mouse spinal cord. Last, the decrease in peak force was restored over time, despite stable and efficient transgene recombination up to 6 months. It is

likely that compensatory mechanisms operated by astrocytes occur but take at least 4 months to be fully established. Yet, we were not able to evidence prominent increase in astrocytic GS to compensate of its loss in OL, at least using immunofluorescence co-staining, with which identifying individual spinal astrocytes in the grey matter is challenging. A precise quantification of GS protein levels in astrocytes would have required complex additional experiments either by breeding the astrocyte reporter *Aldh1L1-eGFP* with *CNP-cre: Glul* $^{fl/fl}$ mice or intraspinal injections of astrocyte-targeted viral vectors expressing GFP to get a sparse astrocyte labeling and quantify GS immunoreactivity in individual astrocytes in both *GS* cKO and control mice. Last, sc or snRNAseq could have been used to assess *Glul* transcripts in both astrocytes and mature OL cell populations for precisely dissecting compensatory processes.

What could be the mechanism underlying *GS* cKO transient decrease in peak force? The timing of this behavioral effect coincides with the significant decrease of Gln but no change in Glu levels in spinal cord extracts from *GS* cKO mice as compared to controls. It is possible that ^{1}H-NMR lacks sensitivity to detect changes in Glu levels, which might nonetheless be sufficient to cause functional alterations of glutamatergic transmission (Xin et al., 2019). Indeed, GS is linked to Glu metabolism and plays a key role in neurotransmission. Decreased Glu recycling is expected to decrease the glutamatergic drive in the spinal cord. Indeed, as MN soma are often abutted by grey matter GS^{+} OL, the latter could be involved in recycling Glu from synapses onto MN cell bodies; thus regulating neuronal excitability, as previously shown in the mouse cortex (Battefeld, Klooster, & Kole, 2016). Decreased Glu transmission might specifically affects MN as glutamatergic innervation of MN soma is extensive (Molofsky et al., 2014) and could translate into decreased peak force, which is a sensitive output of MN function, as suggested by our previous work and others (Kelley et al., 2018; Muller et al., 2014). Last, GS is also involved in ammonia detoxification, which is key to prevent hyperammonia neurotoxic effects of (Zhou, Eid, Hassel, & Danbolt, 2020) and is important for the production of glutathione, which has neuroprotective effects in the enteric nervous system (Knauf, Abot, Wemelle, & Cani, 2020). Both of these GS roles could be involved in neuronal dysfunction in the spinal cord but would need to be further investigated. However, a limitation to take into account is that this behavioral effect could result from cumulative effects of GS loss of function in both the CNS and PNS as *CNP-cre* also leads to transgene recombination in Schwann cells and satellite glial cells, which both express GS.

Our study provides new evidence for GS dysregulation in OL in various disease contexts. First, in the *SOD1(G93A)* mouse model of ALS, we showed that there is a disease-stage dependent increased in the number of GS^{+}OL in ventral spinal cord grey matter from presymptomatic to endstage, which correlates with neuroinflammation. This finding is in accordance with a previous study which showed that in *SOD1(G93A),* adult-born grey matter OL accumulate in the ventral spinal cord (Kang et al., 2013). Here, we showed that these accumulating OL still express GS at high levels, despite an almost complete loss of MN. An accumulation of GS-expressing OL throughout disease progression might increase Gln levels, which can be used for subsequent generation of Glu and therefore contribute to pathological excitotoxic mechanisms, which is one of the main hypothesis for underlying neuronal death in ALS (Cleveland & Rothstein, 2001; Philips & Rothstein,

2014). In line with this, pharmacological inhibition of GS lowered brain Gln and Glu levels (Ghoddoussi et al., 2010) and increases survival in *SOD1(G93A)* mice (Bame et al., 2012). We also showed that *GLUL* transcripts levels were increased in remaining OL but not astrocytes in MS-lesioned tissue versus control human leukocortical samples. A previous study reported qualitative changes in Glu metabolism enzymes in human MS lesions by immunohistochemistry (P. Werner, D. Pitt, & C. S. Raine, 2001). They found that GS levels were decreased active and chronic inactive lesions as compared to non-MS white matter. However, they did not show that these MS lesions contained remaining OL, which could explain the loss of OL GS signal. Interestingly, they showed that in ALS white matter, GS expression in OL is maintained, reminiscent of our findings in the *SOD1(G93A)* ALS mouse model, although it is not clear whether these were brain or spinal cord samples. Together, these results suggest that a dysregulation such as maladaptive increase of GS in OL in neurological diseases could impact neuron-glia crosstalk underlying peak force as well as contribute to Glu-mediated pathological mechanisms.

Supplementary Material

Refer to Web version on PubMed Central for supplementary material.

Acknowledgements

We thank S. Fancy for providing *NG2-DsRed* mice (originally developed by A. Nishiyama) and M. Chavali for technical help. We thank Drs. C. Escartin and C. Lobsiger for inputs on the project, critical reading of the manuscript and feedback on figures. This work was supported by: the Wellcome Trust, NIH NINDS (P01NS083513) and ERC Advanced Grant (ERC-2017-ADG) (to D.H.R.); the German Research Foundation (SCHI 1330/1-1), the Hertie Foundation (medMS MyLab, P1180016) and the National Multiple Sclerosis Society (FG-1607-25111 and FG-1902-33617) (to L.S.); NIH NINDS (R01NS102156), NMSS research grant (RG-1701-26630) and Dana Foundation: The David Mahoney Neuroimaging program (to M.M.C.). L.B.H. is currently supported by a Fondation pour la Recherche Medicale fellowship (ARF201909009244).

References

Anlauf E, & Derouiche A (2013). Glutamine synthetase as an astrocytic marker: its cell type and vesicle localization. Front Endocrinol (Lausanne), 4, 144. doi:10.3389/fendo.2013.00144 [PubMed: 24137157]

Avraham O, Deng PY, Jones S, Kuruvilla R, Semenkovich CF, Klyachko VA, & Cavalli V (2020). Satellite glial cells promote regenerative growth in sensory neurons. Nature communications, 11(1), 4891.

Battefeld A, Klooster J, & Kole MH (2016). Myelinating satellite oligodendrocytes are integrated in a glial syncytium constraining neuronal high-frequency activity. Nat Commun, 7, 11298. doi:10.1038/ncomms11298 [PubMed: 27161034]

Bernstein HG, Bannier J, Meyer-Lotz G, Steiner J, Keilhoff G, Dobrowolny H, … Bogerts B (2014). Distribution of immunoreactive glutamine synthetase in the adult human and mouse brain. Qualitative and quantitative observations with special emphasis on extra-astroglial protein localization. J Chem Neuroanat, 61-62, 33–50. doi:10.1016/j.jchemneu.2014.07.003 [PubMed: 25058171]

Blum JA, Klemm S, Shadrach JL, Guttenplan KA, Nakayama L, Kathiria A, … Gitler AD (2021). Single-cell transcriptomic analysis of the adult mouse spinal cord reveals molecular diversity of autonomic and skeletal motor neurons. Nature neuroscience, 10.1038/s41593-020-00795-0.

Cammer W (1990). Glutamine synthetase in the central nervous system is not confined to astrocytes. J Neuroimmunol, 26(2), 173–178. doi:10.1016/0165-5728(90)90088-5 [PubMed: 1688879]

Chiot A, Zaïdi S, ltis C, Ribon M, Berriat F, Schiaffino L, … Boillée S (2020). Modifying macrophages at the periphery has the capacity to change microglial reactivity and to extend ALS survival. Nature neuroscience, 23(11), 1339–1351. [PubMed: 33077946]

Cleveland DW, & Rothstein JD (2001). From Charcot to Lou Gehrig: deciphering selective motor neuron death in ALS. Nat Rev Neurosci, 2(11), 806–819. doi:10.1038/35097565 [PubMed: 11715057]

D'Amelio F, Eng LF, & Gibbs MA (1990). Glutamine synthetase immunoreactivity is present in oligodendroglia of various regions of the central nervous system. . Glia, 3(5), 335–341. [PubMed: 1977699]

Daikhin Y, & Yudkoff M (2000). Compartmentation of brain glutamate metabolism in neurons and glia. J Nutr, 130(4S Suppl), 1026S–1031S. doi:10.1093/jn/130.4.1026S [PubMed: 10736375]

Eelen G, Dubois C, Cantelmo AR, Goveia J, Brüning U, DeRan M, … Carmeliet P (2018). Role of glutamine synthetase in angiogenesis beyond glutamine synthesis. Nature, 561(7721), 63–69. [PubMed: 30158707]

Gong S, Zheng C, Doughty ML, Losos K, Didkovsky N, Schambra UB, … Heintz N (2003). A gene expression atlas of the central nervous system based on bacterial artificial chromosomes. Nature, 425(6961), 917–925. doi:10.1038/nature02033 [PubMed: 14586460]

Gurney ME, Pu H, Chiu AY, Dal Canto MC, Polchow CY, Alexander DD, … et al. (1994). Motor neuron degeneration in mice that express a human Cu,Zn superoxide dismutase mutation. Science, 264(5166), 1772–1775. [PubMed: 8209258]

Haberle J, Gorg B, Rutsch F, Schmidt E, Toutain A, Benoist JF, … Koch HG (2005). Congenital glutamine deficiency with glutamine synthetase mutations. N Engl J Med, 353(18), 1926–1933. doi:10.1056/NEJMoa050456 [PubMed: 16267323]

Hafemeister C, & Satija R (2019). Normalization and variance stabilization of single-cell RNA-seq data using regularized negative binomial regression. Genome biology, 20(1), 296. [PubMed: 31870423]

He Y, Hakvoort TB, Vermeulen JL, Labruyere WT, De Waart DR, Van Der Hel WS, … Lamers WH (2010). Glutamine synthetase deficiency in murine astrocytes results in neonatal death. Glia, 58(6), 741–754. doi:10.1002/glia.20960 [PubMed: 20140959]

Jayakumar AR, & Norenberg MD (2016). Glutamine Synthetase: Role in Neurological Disorders. Adv Neurobiol, 13, 327–350. doi:10.1007/978-3-319-45096-4_13 [PubMed: 27885636]

Kang SH, Li Y, Fukaya M, Lorenzini I, Cleveland DW, Ostrow LW, … Bergles DE (2013). Degeneration and impaired regeneration of gray matter oligodendrocytes in amyotrophic lateral sclerosis. Nat Neurosci, 16(5), 571–579. doi:10.1038/nn.3357 [PubMed: 23542689]

Kelley KW, Ben Haim L, Schirmer L, Tyzack GE, Tolman M, Miller JG, … Rowitch DH (2018). Kir4.1-Dependent Astrocyte-Fast Motor Neuron Interactions Are Required for Peak Strength. Neuron, 98(2), 306–319 e307. doi:10.1016/j.neuron.2018.03.010 [PubMed: 29606582]

Knauf C, Abot A, Wemelle E, & Cani PD (2020). Targeting the Enteric Nervous System to Treat Metabolic Disorders? "Enterosynes" as Therapeutic Gut Factors. Neuroendocrinology, 110 ((1-2)), 139–146. [PubMed: 31280267]

Lappe-Siefke C, Goebbels S, Gravel M, Nicksch E, Lee J, Braun PE, … Nave KA (2003). Disruption of Cnp1 uncouples oligodendroglial functions in axonal support and myelination. Nat Genet, 33(3), 366–374. doi:10.1038/ng1095 [PubMed: 12590258]

Liang SL, Carlson GC, & Coulter DA (2006). Dynamic regulation of synaptic GABA release by the glutamate-glutamine cycle in hippocampal area CA1. J Neurosci, 26(33), 8537–8548. doi:10.1523/JNEUROSCI.0329-06.2006 [PubMed: 16914680]

Marques S, Zeisel A, Codeluppi S, van Bruggen D, Mendanha Falcao A, Xiao L, … Castelo-Branco G (2016). Oligodendrocyte heterogeneity in the mouse juvenile and adult central nervous system. Science, 352(6291), 1326–1329. doi:10.1126/science.aaf6463 [PubMed: 27284195]

Mates JM, Campos-Sandoval JA, Santos-Jimenez JL, & Marquez J (2019). Dysregulation of glutaminase and glutamine synthetase in cancer. Cancer Lett, 467, 29–39. doi:10.1016/j.canlet.2019.09.011 [PubMed: 31574293]

Miller KE, Richards BA, & Kriebel RM (2002). Glutamine-, glutamine synthetase-, glutamate dehydrogenase- and pyruvate carboxylase-immunoreactivities in the rat dorsal root ganglion and peripheral nerve. Brain research, 945(2), 202–211. [PubMed: 12126882]

Molofsky AV, Kelley KW, Tsai HH, Redmond SA, Chang SM, Madireddy L, … Rowitch DH (2014). Astrocyte-encoded positional cues maintain sensorimotor circuit integrity. Nature, 509(7499), 189–194. doi:10.1038/nature13161 [PubMed: 24776795]

Muller D, Cherukuri P, Henningfeld K, Poh CH, Wittler L, Grote P, … Marquardt T (2014). Dlk1 promotes a fast motor neuron biophysical signature required for peak force execution. Science, 343(6176), 1264–1266. doi:10.1126/science.1246448 [PubMed: 24626931]

Norenberg MD, & Martinez-Hernandez A (1979). Fine structural localization of glutamine synthetase in astrocytes of rat brain. Brain Res, 161(2), 303–310. doi:10.1016/0006-8993(79)90071-4 [PubMed: 31966]

Papageorgiou IE, Valous NA, Lahrmann B, Janova H, Klaft ZJ, Koch A, … Kann O (2018). Astrocytic glutamine synthetase is expressed in the neuronal somatic layers and down-regulated proportionally to neuronal loss in the human epileptic hippocampus. Glia, 66(5), 920–933. doi:10.1002/glia.23292 [PubMed: 29350438]

Philips T, & Rothstein JD (2014). Glial cells in amyotrophic lateral sclerosis. Exp Neurol. doi:10.1016/j.expneurol.2014.05.015

Rose CF, Verkhratsky A, & Parpura V (2013). Astrocyte glutamine synthetase: pivotal in health and disease. Biochem Soc Trans, 41(6), 1518–1524. doi:10.1042/BST20130237 [PubMed: 24256247]

Schirmer L, Velmeshev D, Holmqvist S, Kaufmann M, Werneburg S, Jung D, … Rowitch DH (2019). Neuronal vulnerability and multilineage diversity in multiple sclerosis. Nature, 573(7772), 75–82. doi:10.1038/s41586-019-1404-z [PubMed: 31316211]

Stuart T, Butler A, Hoffman P, Hafemeister C, Papalexi E, Mauck WM, … Satija R (2019). Comprehensive Integration of Single-Cell Data. . Cell, 177(7), 1888–1902.e1821. [PubMed: 31178118]

Takasaki C, Yamasaki M, Uchigashima M, Konno K, Yanagawa Y, & Watanabe M (2010). Cytochemical and cytological properties of perineuronal oligodendrocytes in the mouse cortex. Eur J Neurosci, 32(8), 1326–1336. doi:10.1111/j.1460-9568.2010.07377.x [PubMed: 20846325]

Tyagi RK, Azrad A, Degani H, & Salomon Y (1996). Simultaneous extraction of cellular lipids and water-soluble metabolites: evaluation by NMR spectroscopy. Magnetic resonance in medicine, 35(2), 194–200. [PubMed: 8622583]

Werner P, Pitt D, & Raine CS (2001). Multiple sclerosis: altered glutamate homeostasis in lesions correlates with oligodendrocyte and axonal damage. Annals of neurology, 50(2), 169–180. [PubMed: 11506399]

Werner P, Pitt D, & Raine CS (2001). Multiple sclerosis: altered glutamate homeostasis in lesions correlates with oligodendrocyte and axonal damage. Ann Neurol, 50(2), 169–180. [PubMed: 11506399]

Wishart DS, Feunang YD, Marcu A, Guo AC, Liang K, Vázquez-Fresno R, … Scalbert A (2018). HMDB 4.0: the human metabolome database for 2018. Nucleic acids research, 46(D1), D608–D617. [PubMed: 29140435]

Xin W, Mironova YA, Shen H, Marino RAM, Waisman A, Lamers WH, … Bonci A (2019). Oligodendrocytes Support Neuronal Glutamatergic Transmission via Expression of Glutamine Synthetase. Cell Rep, 27(8), 2262–2271 e2265. doi:10.1016/j.celrep.2019.04.094 [PubMed: 31116973]

Yuen TJ, Silbereis JC, Griveau A, Chang SM, Daneman R, Fancy SP, … Rowitch DH (2014). Oligodendrocyte-encoded HIF function couples postnatal myelination and white matter angiogenesis. Cell, 158(2), 383–396. doi:10.1016/j.cell.2014.04.052 [PubMed: 25018103]

Zhou Y, Eid T, Hassel B, & Danbolt NC (2020). Novel aspects of glutamine synthetase in ammonia homeostasis. Neurochemistry international(140), 104809. [PubMed: 32758585]

Zhu X, Bergles DE, & Nishiyama A (2008). NG2 cells generate both oligodendrocytes and gray matter astrocytes. Development 135(1), 145–157. [PubMed: 18045844]

Main points

- Glutamine synthetase (GS) is expressed in oligodendrocytes (OL) of the mouse and human spinal cord
- OL-specific loss of function causes transient decrease in peak force
- GS expression in OL is altered in chronic pathological conditions

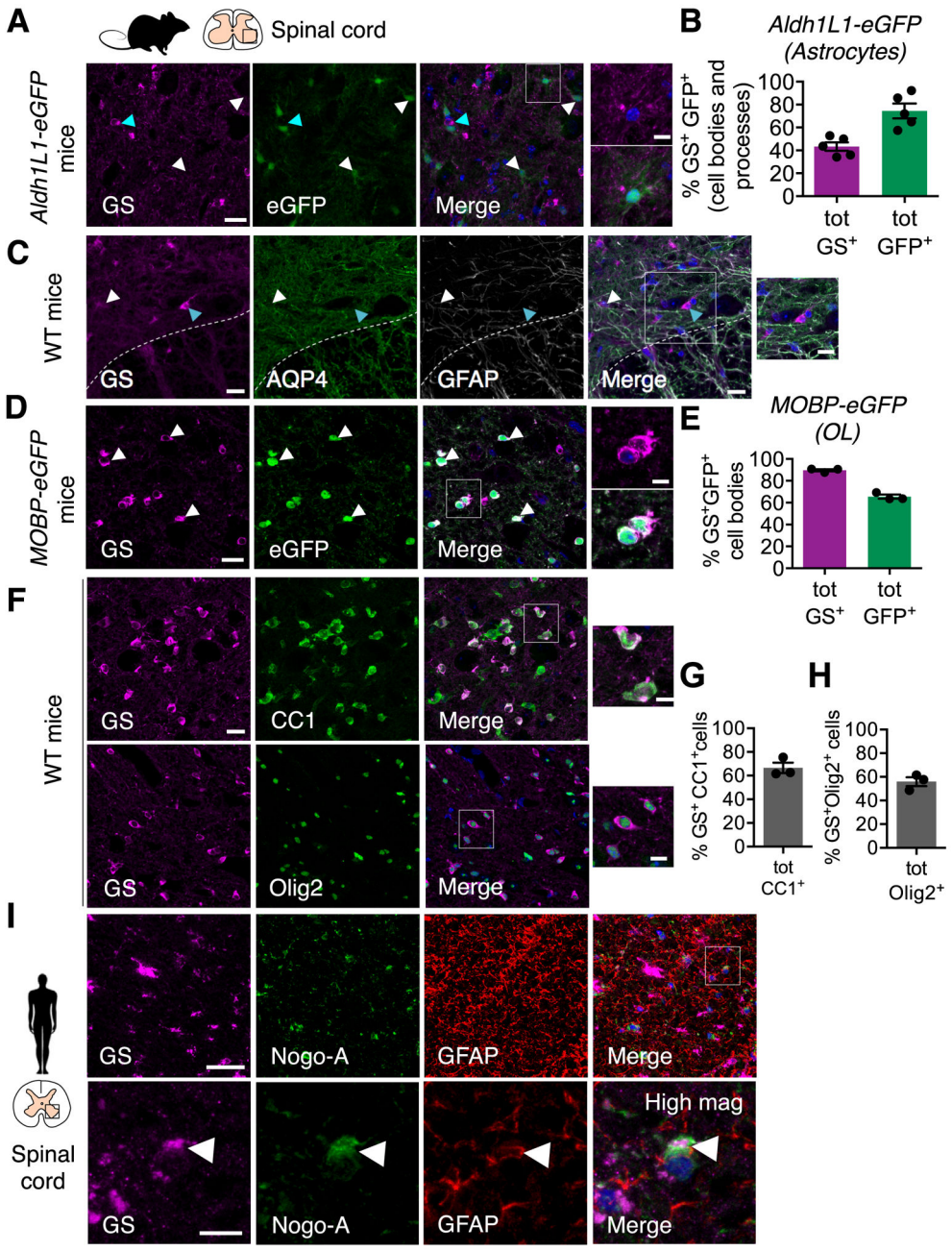

Figure 1. GS is expressed in astrocytes and mature OL in the mouse and human spinal cord.

A, Confocal images of spinal cord sections from astrocyte reporter *Aldh1L1-eGFP* mice immunostained with GS (magenta) and DAPI (blue) (white arrowheads and high magnification). Many cells with high somatic GS^+ signal do not express *Aldh1L1-eGFP* (cyan arrowheads). **B**, Quantification of the % of GS^+ astrocyte cell bodies relative to total GS^+ cells and total *Aldh1L1-eGFP*$^+$ astrocyte cell bodies in the ventral spinal cord grey matter. **C**, Confocal images of spinal cord sections from adult WT mouse spinal cord co-immunostained with GS (magenta), astrocyte markers AQP4 (green), GFAP (white) and DAPI (blue). **D**, Confocal images of spinal cord sections from OL reporter *MOBP-eGFP*

mice immunostained with GS (magenta) and DAPI (blue) showing that a majority of *MOBP-eGFP*$^+$ OL cell bodies express GS (white arrowheads and high magnification). **E**, Quantification of the % of GS$^+$ OL cell bodies relative to total GS$^+$ cell population (astrocytes and OL) and the total *MOBP-eGFP*$^+$ OL cell population in the ventral spinal cord grey matter. **F**, Confocal images of spinal cord sections of adult WT mice co-stained with GS (magenta) and OL markers CC1 (green) (top) and Olig2 (nuclear, green) (bottom) with DAPI (blue) showing that GS is expressed in CC1$^+$ and Olig2$^+$ OL. **G, H**, Quantification of the % GS$^+$CC1$^+$/total CC1$^+$ (**G**) and GS$^+$Olig2$^+$/total Olig2$^+$ cells (**H**). **I**, Confocal images of spinal cord sections from an adult human control (representative image selected from three control spinal cord cross-sections) immunostained with GS (magenta), the OL marker NOGO-A (green), the astrocyte marker GFAP (red) and DAPI (blue). Scale bars: 20μm (**A**-**F**), 40μm (**I**, top), 10μm (**A,** high magnification and **I**, bottom).

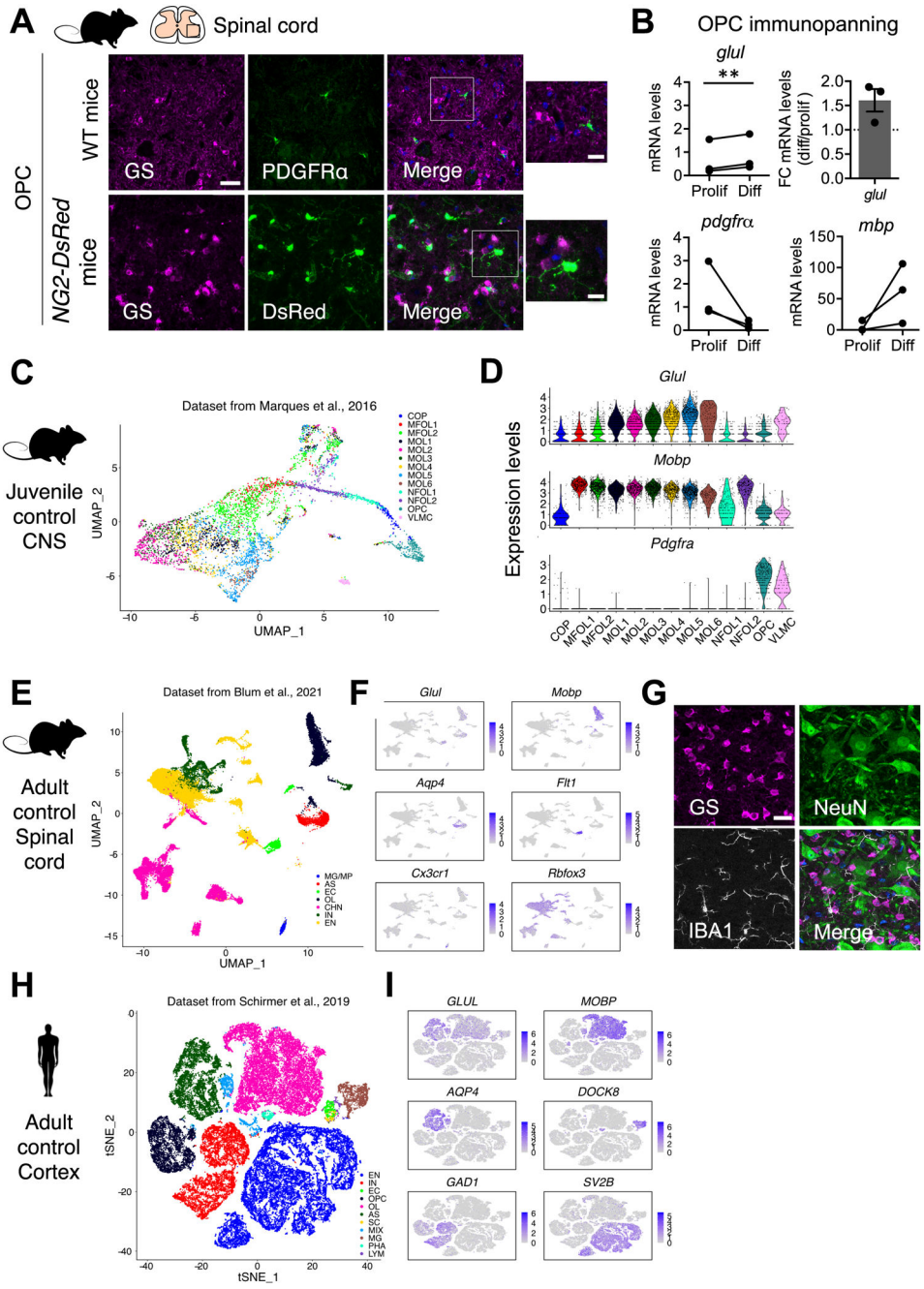

Figure 2. Spinal cord GS expression is macroglial-specific.

A, Immunofluorescence co-staining of GS (magenta) and DAPI (blue) with OPC marker PDGFRα (green) in WT mice and in *NG2-DsRed* OPC reporter mice. **B**, mRNA levels and fold change (FC) of *Glul* (GS-encoding gene) between the proliferation (prolif, OPCs) and differentiation (diff, OL) conditions. *Pdgfra* and *Mbp* were used as positive control markers for proliferation (OPCs) and differentiation (OL) conditions. Data are expressed as mean ± SEM (n = 3 technical replicates). Paired t-test (t = 11.34, df =2), $p < 0.001$.**C,** Uniform Manifold Approximation and Projection (UMAP) plot depicting 5053 cells partitioned into 13 cell type and subtype clusters. VLMC: vascular and leptomeningeal cells, OPC:

Oligodendrocyte progenitor cells, COP: Oligodendrocyte precursor, NFOL: newly formed OL, MFOL: Myelin-forming OL, MOL: Mature OL. **D**, Expression levels of *Glul*, *Mobp* and *Pdgfra*, in cell clusters identified in **C**. **E,** UMAP depicting 43890 cells partitioned in 7 cell type clusters. MG/MP: microglia/macrophage, AS: astrocytes, EC: endothelial cells, CHN: cholinergic neurons, IN: inhibitory neurons, EN: excitatory neurons. **F**, Average expression of *Glul* and cell-type specific markers *Mobp* (OL), *Aqp4* (AS), *Flt1* (EC), *Cx3cr1* (MG) and *Rfbox3* (all neurons). **G**, Immunofluorescence co-staining of GS (magenta), NeuN (neurons, green) and IBA1 (microglia, white). **H,** SnRNA-seq data set analysis from human control leukocortical samples. UMAP plot depicting 48919 cells partitioned into 11 cell type clusters. Additional cell clusters as above include: SC: Stromal cells, MIX: mixture of glial cells, PHA: phagocytes, LYM: lymphocytes **I**, Expression levels of *GLUL*, and cell type specific marker genes *MOBP* (OL), *AQP4* (AS), *DOCK8* (MG,), *GAD1* (IN), *SV2B* (EN). Scale bars: 20μm (**A, D, G**), 10 μm (**A**, high magnification).

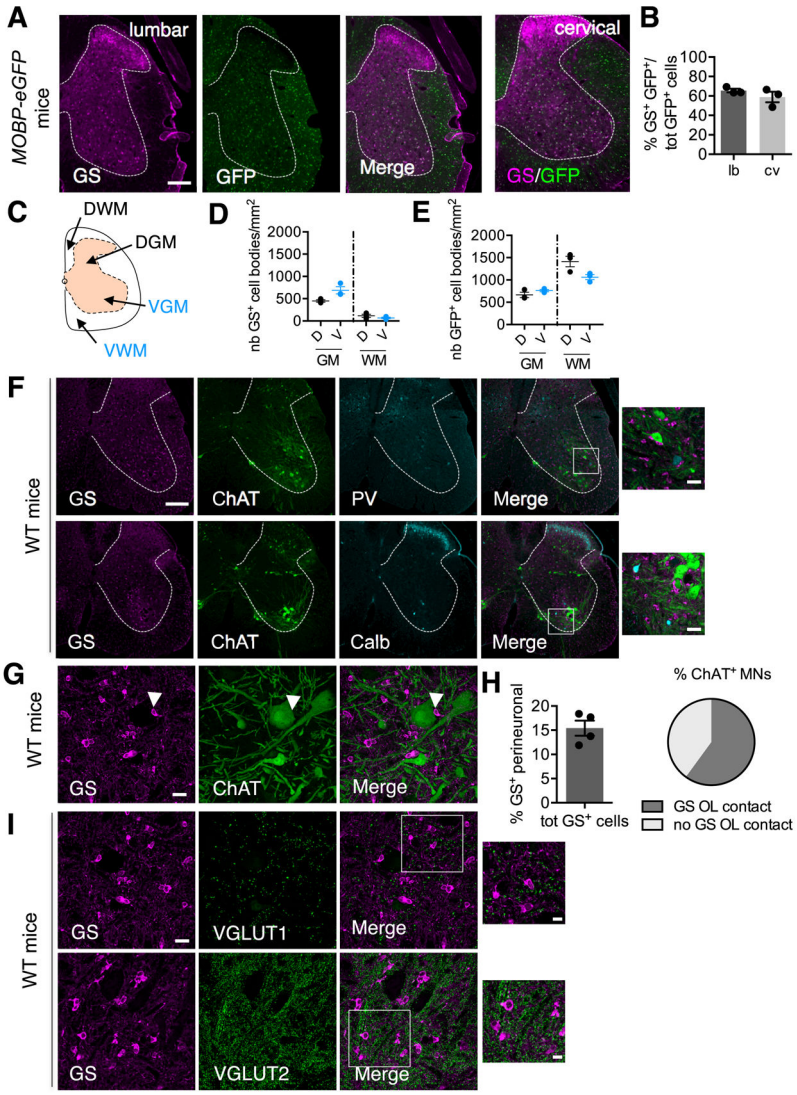

Figure 3. Distribution of GS$^+$ OL in the mouse spinal cord.

A, Low magnification epifluorescence images of spinal cord sections from lumbar (lb, left) and cervical (cv, right) levels from *MOBP-eGFP* mice stained with GS (magenta). **B**, Quantification of the % of GS$^+$OL at the lb and cv spinal cord levels. **C-E,** Regions of interest in the dorsal (D) and ventral (V) grey (G) and white (W) matter (M) that were used to quantify GS (**D**) and GFP (**E**) cell densities. **F**, Confocal images of WT mouse spinal cord sections co-immunostained with GS (magenta), the MN marker ChAT (green) and interneuron markers parvalbumin (PV) and calbindin (Calb) (cyan). **G**, High magnification confocal images of GS (magenta) and ChAT (green) showing GS$^+$ OL perineuronal localization (white arrowhead). **H,** Quantification of the % of GS$^+$ OL with a perineuronal localization and of the % of ChAT$^+$ MN with or without contact with GS$^+$ OL. **I**, Confocal images of fluorescent co-staining of GS (magenta) and glutamatergic terminals (VGLUT1 and VGLUT2, green). Data are expressed as mean ± SEM (n=3-4 mice). Scale bars: 200µm (**A**, **F**), 20µm (**F**, high magnification, **G, I**), 10µm (**I**, high magnification).

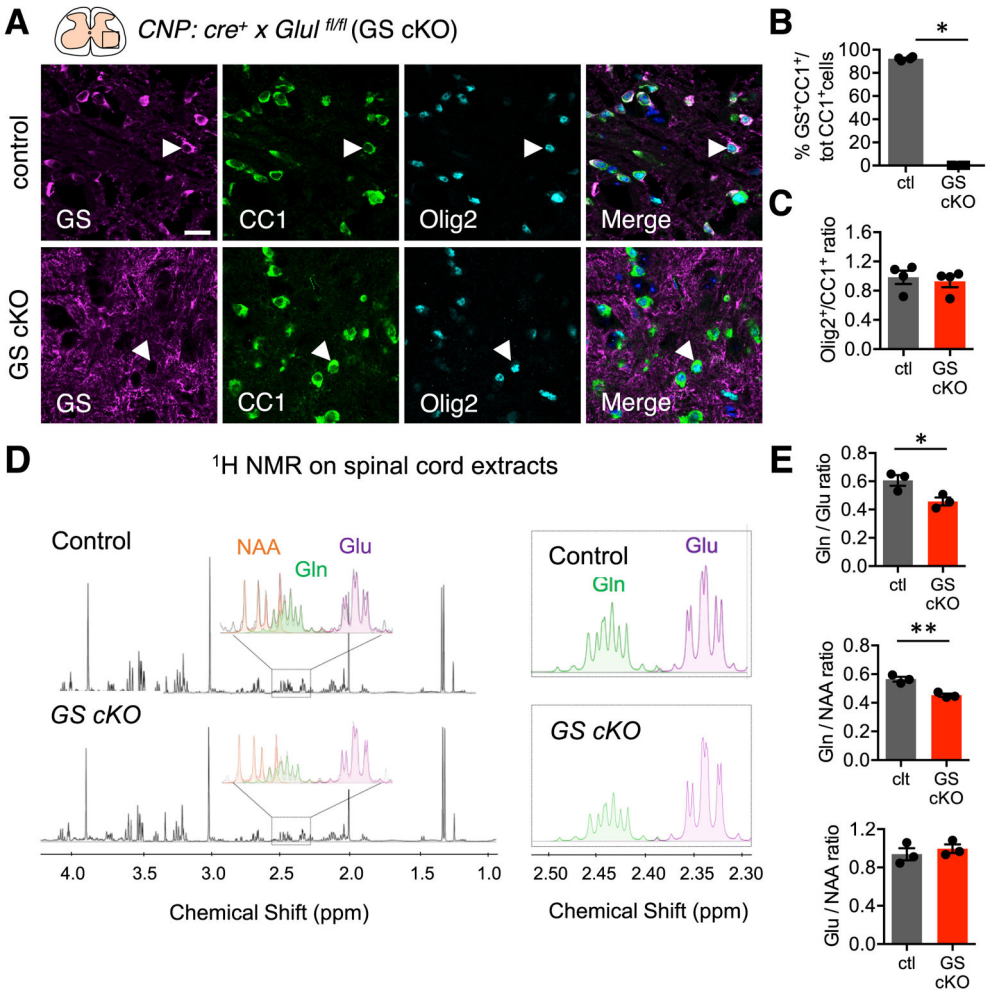

Figure 4. OL specific GS loss-of-function decreases Gln but not Glu levels in spinal cord extracts.

A, Confocal images of spinal cord sections from *CNP-cre*$^{-}$*: Glul* $^{fl/fl}$ (control) and *CNP-cre*$^{+}$*: Glul* $^{fl/fl}$ (*GS* cKO) co-stained with GS (magenta) and OL markers CC1 (green), Olig2 (cyan) and DAPI (blue). **B**, Quantification of the % GS^{+}CC1^{+}/ tot CC1^{+} cells showing the drastic loss of GS expression in CC1^{+} OL. Data are expressed as mean ± SEM (n=4 mice/group). Mann-Whitney test, $p < 0.05$. **C**, The Olig2^{+}/CC1^{+} ratio, an index of OL differentiation is not different in 1 month-old (mo) *GS* cKO as compared to controls. **D**, Representative ^{1}H NMR spectra showing relative abundance of metabolites from spinal cord extracts from 2 mo controls (top) and *GS* cKO (bottom) mice. NAA: N-acetyl-aspartate, Gln: glutamine, Glu: glutamate. **E**, Quantification of the Gln/Glu, Gln/NAA and Glu/NAA ratios in *GS* cKO and control mice. Data are expressed as mean ± SEM (n=3 mice/group). Unpaired t-test (Gln/Glu ratio: $t = 3.159$, $df = 4$, $^{*}p < 0.05$; Gln/NAA ratio: $t = 5.617$, $df = 4$, $^{**}p < 0.01$).

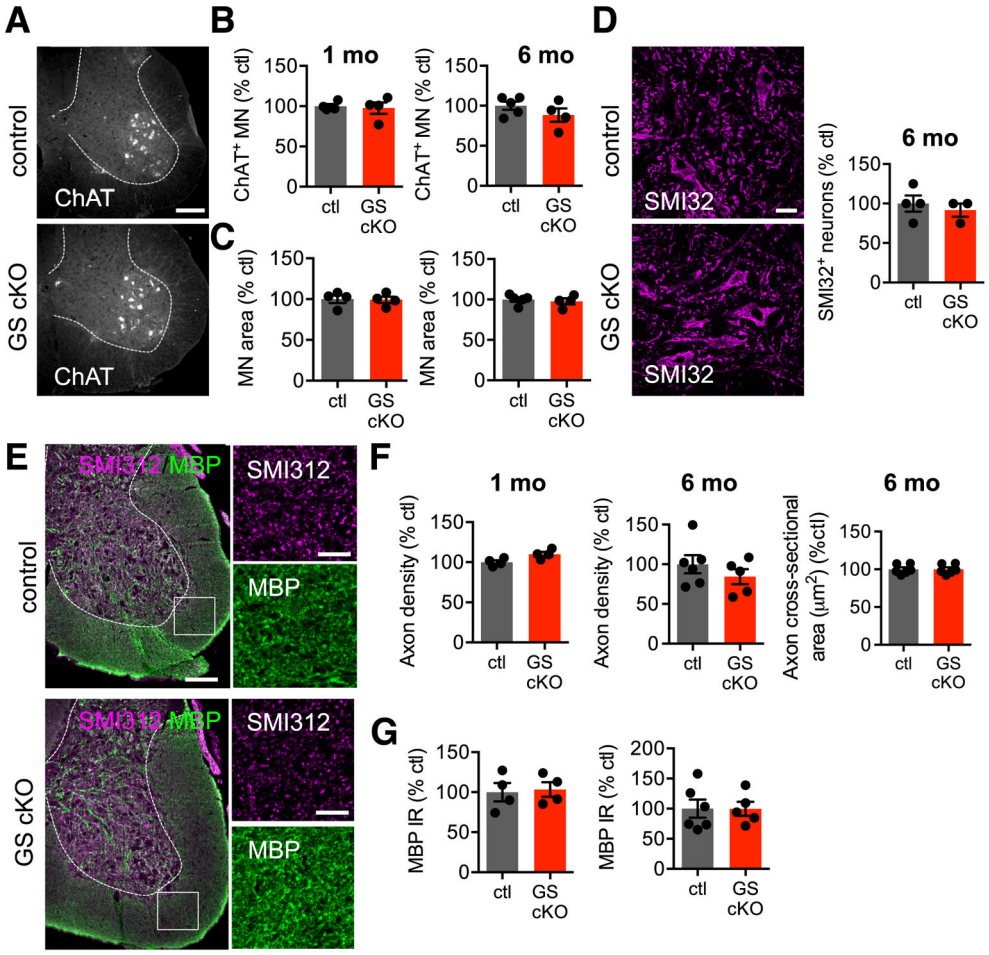

Figure 5. Loss of GS function in spinal OL does not lead to detectable histological changes from 1 to 6 months of age.

A, Low magnification epifluorescence images of spinal cord sections from controls and *GS* cKO immunostained with the MN marker ChAT. **B**, **C**, Quantifications of the number (**B**) and the area (**C**) of ChAT^{+} MN in 1 and 6 mo mice. **D,** Immunofluorescence detection of the neuronal marker SMI32. **E,** Images of spinal cord sections from controls and *GS* cKO immunostained with the pan axonal marker SMI312 (magenta) and the myelin marker MBP (green). **F-G,** Quantification of axon density and cross-sectional area (**F**) and MBP immunoreactivity (**G**) in 1 and 6 mo mice. Data are expressed as mean ± SEM (n=4-6 mice/group). Scale bars: 200µm (**A**, **E**, low magnification), 20µm (**D**, **E,** high magnification).

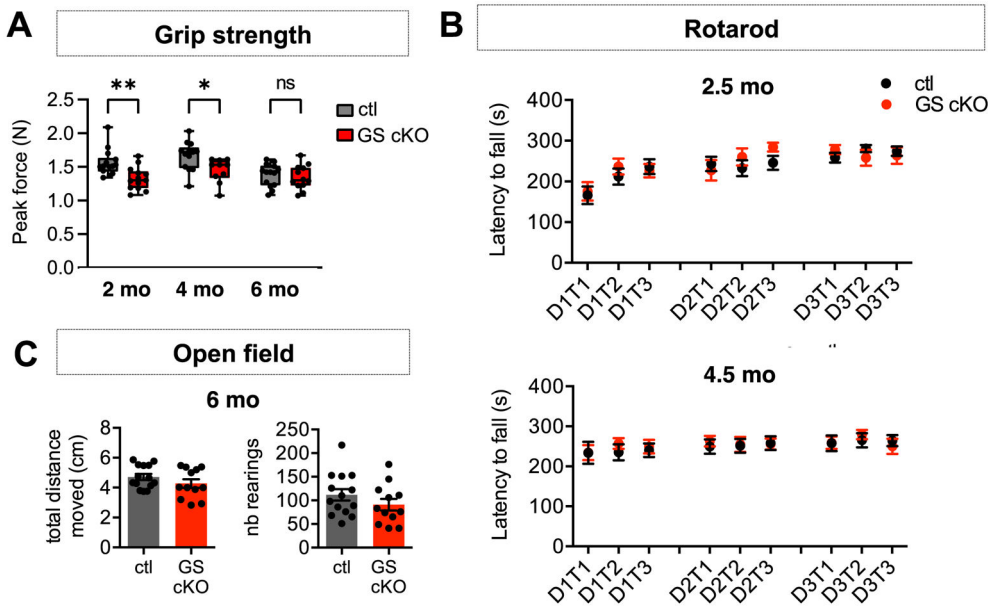

Figure 6. *GS* cKO mice show a transient loss of peak force but otherwise normal motor function. **A**, Forelimb peak force was measured using the grip strength test at 2, 4 and 6 months of age (mo). In box-and-whisker plots, center lines indicate medians, box edges represent the interquartile range, and whiskers extend down to the 10th and up to the 90th percentiles of the distribution (n= 13-14 mice/group). Mixed Effect Model: genotype ($F(1, 25) = 9{,}026$, $p < 0.01$), time ($F(2, 45) = 10{,}50$, $p < 0.001$) and Sidak post hoc *$p < 0.05$, **$p < 0.01$. **B**, Rotarod performances of *GS* cKO and control mice at 2.5 mo (top) and 4.5 mo (bottom). **C,** At the open field test, *GS* cKO mice showed normal total distance moved and number of rearings, as compared to littermate controls at 6 mo.

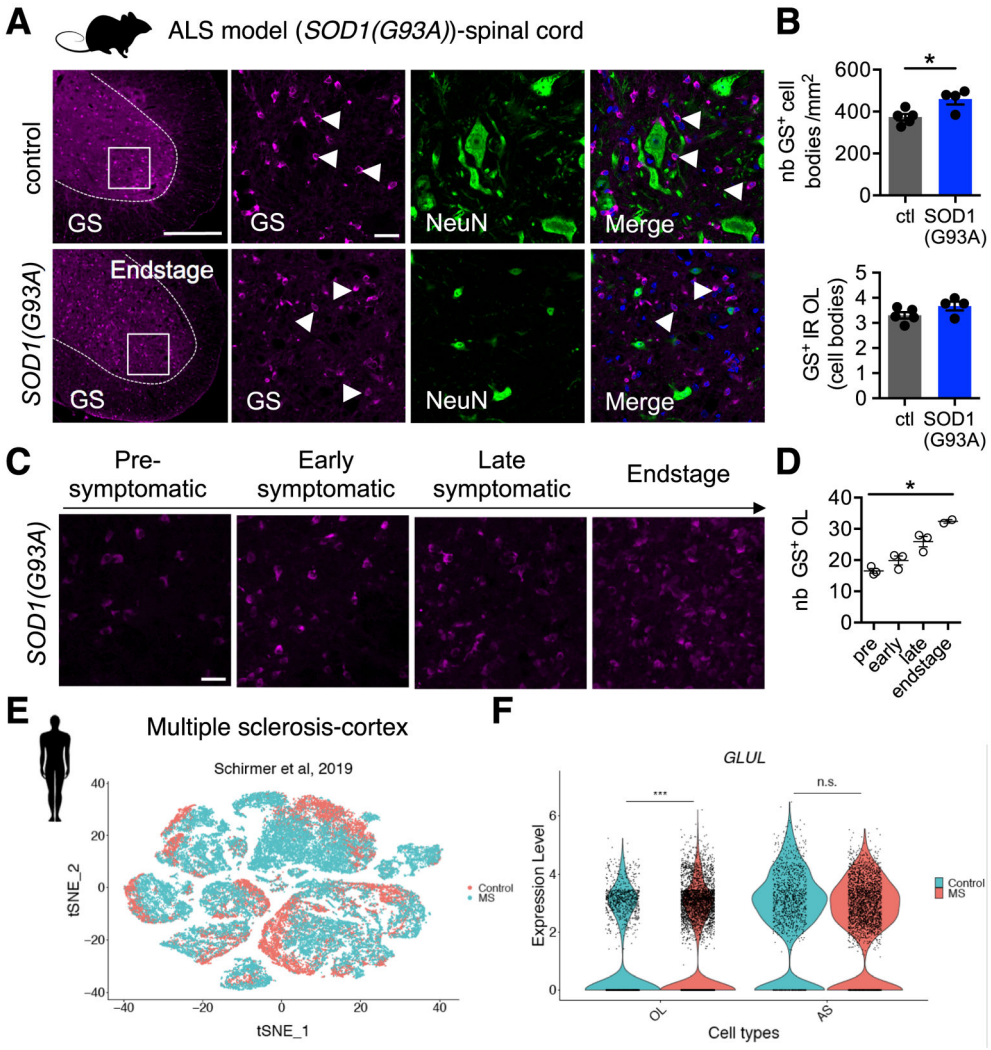

Figure 7. Dysregulation of GS OL in chronic pathological conditions.

A, Low magnification epifluorescence (left) and high magnification confocal (right) images of immunofluorescent co-staining of GS (magenta), NeuN (green) and DAPI (blue) in endstage *SOD1(G93A)* ALS mice and age-matched littermate control mice ventral spinal cord. **B**, Quantification of the number of GS^+ OL cell bodies and GS immunoreactivity. **C**, Confocal images of immunofluorescent GS staining on spinal cord sections from *SOD1(G93A)* mice at different disease stages. **D**, Quantification of the numbers of GS^+ cell bodies according to disease progression. **E**, SnRNA-seq data set analysis from human leukocortical samples from MS and non-MS controls. Uniform Manifold Approximation and Projection (UMAP) plot depicting 48919 cells partitioned into 11 cell type clusters. EN: excitatory neurons, IN: inhibitory neurons, EC: endothelial cells, OPC: oligodendrocyte progenitor cells, OL: oligodendrocytes, MG/MP: microglia/macrophage, AS: astrocytes, SC: Stromal cells, MIX: mixture of glial cells, PHA: phagocytes, LYM: lymphocytes. **F**, Average expression of *GLUL* in OL and AS nuclei populations. Scale bars: 200μm (**A**, low magnification), 20μm (**A**, high magnification, **C**).